OPEN ACCESS

University of BRISTOL

Lu, Q., Liu, L., Leng, J., Scarpa, F., & Liu, Y. (2020). Composite piezoelectric energy harvesters with symmetric angle-ply stacking sequences and variable through-the-thickness Poisson's ratios. *physica status solidi (b)*, *257*(10), [1900689]. https://doi.org/10.1002/pssb.201900689

Peer reviewed version

Link to published version (if available):
10.1002/pssb.201900689

Link to publication record in Explore Bristol Research
PDF-document

This is the author accepted manuscript (AAM). The final published version (version of record) is available online via Wiley at https://onlinelibrary.wiley.com/doi/full/10.1002/pssb.201900689 . Please refer to any applicable terms of use of the publisher.

University of Bristol - Explore Bristol Research
General rights

This document is made available in accordance with publisher policies. Please cite only the published version using the reference above. Full terms of use are available:
http://www.bristol.ac.uk/red/research-policy/pure/user-guides/ebr-terms/

Composite piezoelectric energy harvesters with symmetric angle-ply stacking sequences and variable through-the-thickness Poisson's ratios

Qingqing Lu[1, 2], Liwu Liu[2], Jinsong Leng[1], Fabrizio Scarpa[3, 4 *], Yanju Liu[2, *]

[1]*Centre for Composite Materials, Science Park of Harbin Institute of Technology (HIT), P.O. Box 3011, No. 2 YiKuang Street, Harbin 150080, People's Republic of China*

[2]*Department of Astronautical Science and Mechanics, Harbin Institute of Technology (HIT), P.O. Box 301, No. 92 West Dazhi Street, Harbin 150001, People's Republic of China*

[3]*Bristol Composites Institute (ACCIS), University of Bristol, Bristol, BS8 1TR, UK*

[4]*Dynamics and Control Research Group (DCRG), CAME, University of Bristol, BS8 1TR, UK*

*Corresponding author

Tel./FAX: +86-451-86414825.

E-mail: yj_liu@hit.edu.cn (YJ Liu)

*Corresponding author

Tel./FAX: +44 1173315306

E-mail: f.scarpa@bristol.ac.uk (F. Scarpa).

Abstract

We evaluate in this work the effect of symmetric carbon fiber composites laminates with angle-ply stacking sequences ($[\pm\beta/\pm\theta]_S$) in the design of composite piezoelectric energy harvesters (PEHs). Some of those specific stacking sequences also feature negative Poisson's ratio (NPR) or near zero Poisson's ratio (NZPR) through the thickness for ply angles $\theta < 45^\circ$. We consider here six different architectures all with similar in-plane elastic modulus E_1 and different positive and negative Poisson's ratio v_{13} values. Finite element models are developed to understand the distribution of the voltage density of the laminates with the different stacking sequences and their bending properties. Experimental tests (3-point bending and vibration) are also performed. Both the simulations and the experimental results show that the PEH with the stacking sequences of near zero v_{13} generate the highest power compared with the other composite energy harvesters. The maximum voltage FRFs (Frequency response functions) happens at the fundamental resonance, and the PEH with near zero v_{13} has also the lowest resonance frequency compared to the other stacking sequences.

Keywords

Composite laminates, piezoelectric energy harvester, through-the-thickness Poisson's ratio, auxetic, zero Poisson's ratio.

1. Introduction

Piezoelectric energy harvesting is considered to be an effective technology to supply power in wireless sensor networks [1][2][3]. PEHs can make use of vibration or dynamic environments through direct piezoelectric effect [4][5]. Piezoelectric energy harvesters also feature simple structural designs and high energy conversion factors [6]. The typical structure of a linear PEH consists of an elastic substructure, piezoelectric layers and a tip mass. Erturk and Inman [7][8][9] have developed exact electromechanical solutions for cantilevered piezoelectric energy harvesters (unimorph and bimorph) for undergoing transverse vibrations using Euler-Bernoulli beam models and serial/parallel connections of PZT (Lead zirconate titanate) layers. Buric *et al.* have described a piezoelectric energy harvester for generating power to operate a microcontroller and radio transmitter and acquire sampled machine data [10]. Erturk and Inman have also discussed the energy harvesting potential of general piezoaeroelastic systems [11] and benchmarked different piezoelectric materials for charging batteries [12]. An interesting application has been presented by Aktakka *et al.*, with the design, fabrication and testing of a PEH that generated power from the tethered flight of a beetle [13]. For PEH systems under linear elastic regime, the maximum voltage only occurs at the resonance of the beams, and several researchers have devoted significant efforts to improve the general performance of the harvesters. Shahruz has designed a series of mechanical band-pass filters consisting in an ensemble of cantilever beams with different physical parameters and tip masses [14]. Xue *et al.* have also described broadband piezoelectric harvesters by integrating multiple cantilevers with

different aspect ratios [15]. Qi *et al.* have investigated the performance of a clamped-clamped piezoelectric beam with side mounted cantilevers with wide band energy harvesting characteristics [16]. An internal resonance- based broadband vibration energy harvester has been proposed by Xiong *et al* [17]; compared to conventional energy harvesters, the natural frequencies of the internal resonance system could be easily adjusted to obtain more resonant peaks. Some other nonlinear PEH designs have been presented, featuring magnets or nonlinear restoring forces to expand the working bandwidth of traditional linear PEH systems [18][19][20][21]. Materials with anisotropy have also been evaluated to fabricate PEH cantilever beams. Arrieta *et al.* have fabricated a nonlinear PEH plate with carbon fiber/epoxy bistable composites [22]. Shi *et al.* have investigated new ways to integrate piezoelectric energy harvesting elements into carbon fiber composite structures and complex geometry airframe [23]. An investigation on the energy harvesting generated by the dynamic bending response of a composite wing box with embedded piezoelectric actuators has been presented by Akbar and Curiel-Sosa [24]. Paknejad *et al.* have developed a distributed parameter model of various multilayer composite beams with piezoelectric energy harvesters and discussed the effect of various composite laminate architectures [25]. Broader composite/PZT PEH architectures and related performance benchmarking have been also developed by Liu et al [26]. Particular stacking sequences and architectures of the composite beams produce variable stiffness and through-the-thickness Poisson's ratio, some of them auxetic (negative Poisson's ratio). Example of auxetic materials and structures are molecular systems [27] (chirality of hard [28] and soft [29] hexamers),

foams [30][31][32][33][34], honeycombs [35][36][38] and adaptive structures [39][40][41]. Piezoelectric and auxetics have also been considered in hydrophone composites [42][43][44] and lattices [45][46]. They have been extensively studied both theoretically ([47]-[51]) and experimentally ([52]-[55]) for the past three decades. Auxeticity has also been identified at nanoscale in graphene systems [56][57]. More information and developments about auxetics and anomalous systems can be found in [58][59]. The main outcome from the latter studies was that the presence of a negative Poisson's ratio in composite hydrophones significantly increased the electromechanical coupling and acoustic sensitivity of the devices, while NPR lattices allowed an enhanced control of the wave evanescence through distributed piezoelectric patches. Those are only some examples of the potential advantages of using auxetics, ranging from enhanced indentation resistance and energy absorption, tailorable acoustic signature and adaptability to complex and morphing shapes. Composites with stacking sequences showing negative Poisson's ratios have been developed by Herakovitch [60], Sun and Li [61], Clarke *et al.* [62], Evans *et al* [63], Alderson *et al.*[64]. While Peel and Jensen first [37] and then Chen *et al* have evaluated stacking sequences with auxetic and variable Poisson's ratio composites with elastomeric matrices [65], Harkati *et al.* have evaluated the influence of different types of carbon reinforcement, resin and fiber volume fractions on the through-the-thickness Poisson's ratio of laminates [66]. Bezazi *et al.* have also investigated the static and cyclic fatigue behavior of auxetic carbon/epoxy composites [67]. Zero Poisson's ratio is also a mechanical feature that has attracted attention [68][69][70], in particular for the development of structures with

single radius curvature and uni-directional and 2D morphing configurations [40][71][72][73].

In this study we aim to explore and discuss the potential influence on the static, dynamic and energy harvesting behavior of the $[\pm\beta/\pm\theta]_S$ architecture in symmetric angle-ply laminates architecture as piezoelectric composite energy harvesters. With variable stacking sequences one can obtain laminates with through-the-thickness Poisson's ratios exhibiting NPR or near zero values, and this part is evaluated by using classical laminate theory (CLT), as adopted in previous works. Several stacking sequences with different through-the-thickness Poisson's ratios are then selected to fabricate composite beams with PZT layers. The static response of the composite beams is initially evaluated with three-point bending tests, and finite element models of the beams including the presence of PZT patches are also developed. The influences of the stacking sequences over the stiffness and voltage output at resonance are studied through numerical simulations and experiments.

The numerical and experimental results presented in this paper show that the PEHs with NZPR generate the highest power compared to the other configurations, and auxetic through-the-thickness composites PEHs also offer higher weighted specific output voltages that more classical symmetric laminate architectures.

2. Laminate analysis

2.1. Symmetric laminate model

We recall here the approach introduced by Herakovich [60] to evaluate the through-the-thickness Poisson's ratio of elastic anisotropic plates. For laminates with symmetric

stacking sequences (Figure 1), the relationship between strain and axial force can be given as:

$$\begin{Bmatrix} \varepsilon_1 \\ \varepsilon_2 \\ \varepsilon_3 \end{Bmatrix} = \begin{bmatrix} A_{11} & A_{12} & A_{16} \\ A_{12} & A_{22} & A_{26} \\ A_{16} & A_{26} & A_{66} \end{bmatrix}^{-1} \begin{Bmatrix} N_1 \\ N_2 \\ 0 \end{Bmatrix} \tag{1}$$

The matrix A_{ij} is defined by:

$$A_{ij} = \sum_{k=1}^{N} Q_{ij}^{k} t^{k} \tag{2}$$

In Eq. (2), N is the number of plies, Q_{ij}^{k} is the stiffness coefficient and t^{k} is the thickness of *k*th layer. The through-the-thickness Poisson's ratio v_{13}, v_{23} are defined as:

$$v_{13} = -\frac{\varepsilon_{x_3}}{\varepsilon_{x_1}}, v_{23} = -\frac{\varepsilon_{x_3}}{\varepsilon_{x_2}} \tag{3}$$

The equations of v_{13}, v_{23} can be found in Ref. [7]:

$$\begin{aligned} v_{13} &= -\frac{1}{2h(A_{11})^{-1}} \begin{Bmatrix} (A_{11})^{-1} \\ (A_{12})^{-1} \\ (A_{16})^{-1} \end{Bmatrix} \left[\sum_{k=1}^{N} (S'_{31} S'_{32} S'_{36}) \begin{pmatrix} Q'_{11} \\ Q'_{12} \\ Q'_{16} \end{pmatrix} t^{k}, \sum_{k=1}^{N} (S'_{31} S'_{32} S'_{36}) \begin{pmatrix} Q'_{12} \\ Q'_{22} \\ Q'_{26} \end{pmatrix} t^{k}, \sum_{k=1}^{N} (S'_{31} S'_{32} S'_{36}) \begin{pmatrix} Q'_{16} \\ Q'_{26} \\ Q'_{66} \end{pmatrix} t^{k} \right] \\ v_{23} &= -\frac{1}{2h(A_{22})^{-1}} \begin{Bmatrix} (A_{21})^{-1} \\ (A_{22})^{-1} \\ (A_{26})^{-1} \end{Bmatrix} \left[\sum_{k=1}^{N} (S'_{31} S'_{32} S'_{36}) \begin{pmatrix} Q'_{11} \\ Q'_{12} \\ Q'_{16} \end{pmatrix} t^{k}, \sum_{k=1}^{N} (S'_{31} S'_{32} S'_{36}) \begin{pmatrix} Q'_{12} \\ Q'_{22} \\ Q'_{26} \end{pmatrix} t^{k}, \sum_{k=1}^{N} (S'_{31} S'_{32} S'_{36}) \begin{pmatrix} Q'_{16} \\ Q'_{26} \\ Q'_{66} \end{pmatrix} t^{k} \right] \end{aligned} \tag{4}$$

where S'_{ij} are the coefficients of the transformed compliance matrix.

Laminates with symmetrical configurations of the type $[\pm\beta / \pm\theta]s$ are considered for their large variation of through-the-thickness Poisson's ratio, with large negative values. For a particular geometric representation of the stacking sequence the reader is referred to [39]. The number of carbon fiber composite laminas is 8 and increments of 5 degrees are considered. The mechanical properties, including the elastic modulus E_1, bending

stiffness D_{11} and Poisson's ratio v_{13}, v_{23} are calculated by the Autodesk Helius Composites 2017 (Composites design software, Autodesk).

2.2. The mechanical simulation of laminates with different stacking sequences

The laminas are represented by unidirectional IM7/8552 (Hexcel Composites, USA - Table 1). The stacking sequences are illustrated in Table2. The ply angle θ increases with 5° from 0° to 90°.

The elastic modulus along the x_1-direction E_1 and the reduced bending stiffness D_{11} for the different stacking sequences are shown in figure 2. The ply angle β is increased from ST1 to ST12, and the increase of β leads to a smooth decrease of E_1 when $\beta \leq 45^\circ$ and low and intermediate θ values ($15^o < \theta < 60^o$). After this angle the modulus E_1 increases, but slowly. For $\theta = 0^\circ$, the analytical estimate of E_1 for the ST1 sequence ($[\pm 10^\circ / \pm\theta]_s$) is 134*GPa,* while in the case of the laminate $[\pm 45^\circ / \pm 0^\circ]_s$ (ST-8) the modulus is reduced to 79.3*GPa*. The bending stiffness D_{11} is also decreased with the increase of the ply angles β and θ, however the value of D_{11} is more sensitive to the variation of β.

Figure 3 shows the analytical estimations for the in-plane Poisson's ratio v_{12} versus the different staking sequence configurations and angles θ. For increasing ply angles β, the magnitude of the Poisson's ratio first increases then decrease and is always positive. The maximum value occurs at the ply angle β equal to 25° and the minimum value occurs for larger β values ($\beta = 80^\circ$).

Figures 4 (a)-(b) show the analytical estimates related to the through thickness Poisson's ratios versus the ply angles $[\pm\beta / \pm\theta]_S$ at different tacking sequences. With

the increase of the ply angle β, the magnitude of v_{13} first decreases (from ST1 to ST4), then increase moving from ST5 to ST12. Some specific stacking sequences feature NPR, such as ST1 at $\theta = 30^{\circ}$ and ST2 for $\theta = 20^{\circ} \sim 35^{\circ}$. One can notice that the NPR or NZPR effects occur around ply angles $\theta < 45^{\circ}$, after which v_{13} returns to positive values. The response of the Poisson's ratio v_{23} is symmetric to the one of v_{13}, with NPR occurring for $\theta > 45^{\circ}$ and $\beta > 50^{\circ}$ (stacking sequences ST9 to ST12). In this study, the composite laminates are designed as beam, which mean the length of the beam is relatively larger than the width, so the Poisson's ratio v_{13} is mainly conserided.

2.3. Finite element analysis

In order to understand more in depth the differences between positive and negative v_{13} laminates, we select six different stacking sequences with almost equal (or as close as possible) 1-direction elastic modulus E_1 (Table 3).

The finite element model of the composites beam is developed using the Abaqus/CAE 6.12-1 (3DS Dassault Systems, France) (Figure 5). The CFRP (Carbon fiber reinforced polymer) laminates are modeled using 4-nodes S4R composite shells, while the piezoelectric layer is represented by piezoelectric C3D8E linear elements. The polarization of the piezoelectric layer is along the z-axis, and the bottom nodes are set to zero electric potential. Mesh sizes of the PZT layer of 0.2mm along the length and width, and of 0.025mm through-the-thickness provide both a convergence on forces and voltages. Similar mesh dimensions are used for the composites part. The properties of the PZT layer are listed in Table 4.

The boundary conditions of the beams correspond to the ones of a 3-points bending test

(standard ASTM D790), with the load applied on the center. The length of the CFRP beam is 100mm and the support span is 70mm. After the application of a load (10*N*), the voltage is obtained following a two steps process. A zero-electric potential at the bottom surface of the PZT and the mechanical boundary conditions plus the load are applied to the finite element model in the initial step. The resulting electrical potential is then stored in the EPOT (Electrical Potential) in the output results. The middle point of the top surface of the PZT layer is the origin of the Cartesian coordinate system (figure 5). The z-axis in here is directed from the top to the bottom surface of the PZT; the voltage distribution along the three Cartesian directions can then be read.

Figure 6 represents the maximum voltage along the z-direction (through-the-thickness) with the different stacking sequences considered. The laminates exhibiting NZPR have the highest voltage output, and at the same time possess the highest compliance (i.e., lowest bending stiffness, see Table 6). The laminates with negative v_{13} can however generate more power than the ones with positive through-the-thickness Poisson's ratio. For example, when selected stacking sequences with close in-plane Young's modulus E_1 ($[\pm 25^\circ / \pm 25^\circ]_s$, $E_1 = 68.8GPa$; $[\pm 15^\circ / \pm 90^\circ]_s$, $E_1 = 67.2GPa$; $[\pm 20^\circ / \pm 30^\circ]_s$, $E_1 = 70.2GPa$; $[\pm 10^\circ / \pm 60^\circ]_s$, $E_1 = 70.5GPa$), the maximum voltage generated by the laminates $[\pm 25^\circ / \pm 25^\circ]_s$ ($v_{13} = -0.176$) is 1.6V, which is 28% higher that the positive v_{13} stacking sequence ($[\pm 15^\circ / \pm 90^\circ]_s$, $v_{13} = 0.428$). Yet, the largest voltage (2.75V) along the z-direction is generated by the near zero v_{13} laminate with the ($[\pm 40^\circ / \pm 15^\circ]_s$) configuration.

The size of the PZT layer used in the finite element analysis (FEA) simulation is 40mm

of length and 10mm of width. To better take into account effects provided by the relative dimensions and mass of the PZT layer we consider a metrics involving the voltage density (d_V) of the through-the-thickness section in the following manner:

$$d_V = \frac{V_{max}+V_{min}}{2h} \tag{5}$$

Here, the maximum electric potential V_{max} occurs on the top surface of the PZT, and V_{min} is the electric potential of the bottom of the piezoelectric patch. Four different size PZT layers are analyzed, and the results of the voltage density divided by D_{11}/m_{pzt} [26] are calculated under a $10N$ load (Figure 7). In this way the voltage density is weighted by the specific stiffness of the laminate, taking the mass of the PZT layer as reference. The results show that the width of the PZT can affect significantly the voltage density of the laminates. The voltage densities of the composites with NZPR are higher than the ones produced by the other stacking sequences. For example, the density of the laminate with 40mm length and 10mm width at $\nu_{13} = -0.011$ ($[\pm 40^\circ / \pm 15^\circ]_s$) is $0.19\,V\mathrm{g}/kN/mm^3$, while for 40mm of length and 20mm of width the same voltage density is reduced by 4.3 times ($0.043\,V\mathrm{g}/kN/mm^3$). These simulations show that the laminates with near zero or negative ν_{13} possess better power generation performances than analogous composites with positive ν_{13}.

2.4. Vibration FRF simulations

The vibration response of the composites beam is analyzed based on the FE model presented in figure 5. The boundary conditions during the vibration simulation are changed to be clamped-free and the effectively length of the cantilever beam is effectively 80mm. The analysis is performed using the shell element SR4 (doubly

curved shell elements with 4-nodes per element) for the CFRP and the C3D8E (An 8-node linear piezoelectric brick) for the PZT layer. Firstly, the natural frequencies of the composites beam with different stacking sequences are simulated. The step type is "frequency" with Subspace Eigensolver and the first mode natural frequency will be solved. After the simulation of the natural frequencies, the vibration of the composites beam at corresponding natural frequencies are progressed. We use the step of the Dynamic-Implicit to simulate the vibration of the cantilever beam. The excitation is applied with dynamic displacement and the relationship between the displacement and the excitation acceleration and frequency is $A = 0.004Df^2$, where A is the excitation acceleration, D is the excitation displacement and f is the frequency. During the simulation, the excitation acceleration is equal to 1g. The excitation displacement can be calculated then applied on the left part of the beam.

The damping of the beam is applied with Rayleigh damping, which can be expressed as:

$$\zeta = \frac{\alpha}{2\omega} + \frac{\beta\omega}{2} \tag{6}$$

where ζ is the damping ratio, α is the mass-proportional damping coefficient, β is the stiffness-proportional damping coefficient (not to be confused here with the angle of the stacking sequence). Then the coefficients can be obtained:

$$\begin{cases} \alpha = \dfrac{2\omega_1\omega_2\zeta}{\omega_1+\omega_2} \\ \beta = \dfrac{2\zeta}{\omega_1+\omega_2} \end{cases} \tag{7}$$

In (7) ω_1 and ω_2 are the natural frequencies of the reference modes. For the cantilever beam, $\omega_2 = 4.679/1.875\omega_1$. The calculated coefficients are applied on the material properties of the CFRP and PZT. The FEA result is shown in figure 8. The laminates

with near zero ν_{13} ($[\pm 40^\circ / \pm 15^\circ]_s$, $[\pm 35^\circ / \pm 15^\circ]_s$) show the highest values of output voltage (11.2V/g at 112.2Hz, 10.7V/g at 124.3Hz) compared to the values of the other four stacking sequences. The maximum voltage FRF of the $[\pm 25^\circ / \pm 25^\circ]_s$ laminate occurs at 148.5Hz with 9.8V/g, while the $[\pm 20^\circ / \pm 30^\circ]_s$ laminates can generate 8.2V/g at 161.2Hz. When the Poisson's ratio ν_{13} is increased towards positive values, the maximum output voltage decreases to 7.5V/g ($[\pm 15^\circ / \pm 90^\circ]_s$) and 7.1V/g ($[\pm 10^\circ / \pm 60^\circ]_s$) respectively.

Experimental setup

3-points bending experiments

Composites specimens have been fabricated using 8 carbon fiber composite plies ($[\pm\beta / \pm\theta]_S$) and one PZT layer (Sinoceramics Inc., Shanghai, China). The PZT patches are attached to the top surface and located at the center. The dimensions of the PZT layer are 40mm length, 10mm width and 0.2mm thickness. The composite beams have been produced using a Hexcel prepreg IM7/8552 unidirectional carbon/epoxy. The specimens with their different stacking sequences used in this experiment are listed in Table 3.

The plies are sized by using a cutting machine (Gensis 2100, Black & White Ltd) then laid up with the $[\pm\beta / \pm\theta]_s$ stacking sequence (Table 3). The resin inside the prepregs also acts as adhesive for the PZT layers. The curing progress is performed in an autoclave at $125^\circ C$, under a pressure of 1 bar for 16 hours. Here, the pressure is controlled by a vacuum pump connected with the vacuum-bagged specimen. After curing, the plate is cut into specimens of 20mm width with 100mm length. According

to the three-points bending test standard ASTM-D790, the span of the support is 70mm. The tests are performed using a universal testing machine type Instron 8872 equipped with 5KN load cell and crosshead speed of 5mm/min. Each laminate with PZT are test three times (three similar specimens) under the same test conditions.

Vibration experiments

The purpose of the vibration test is to obtain experimental FRF curves to benchmark the model natural frequencies, damping ratios and voltage FRFs for the various stacking sequences configurations. The specimens for dynamic tests are fabricated following the same procedure related to the three-points bending specimens, however with clamped-free boundary conditions in this case.

The experimental setup is shown in figure 9. The specimen is held by a metal clamp and mounted on the surface of a shaker (MPA407/M437M, ETS Inc.), which is controlled by VENZO880 shaker control system (Dyna tronic Corporation) and power amplifier (IPA60H/ M437A, ETS Inc.). The sensors are an accelerometer (CA-YD-108, Sinocera Piezotronics Inc.) and single point laser Doppler vibrometer (VibroMet model 500V, Metrolaser Inc.). The velocity signal has been FFT-transformed with a sampling frequency of 4096Hz and a Hanning windowing to reduce the spectral leakage. The accelerometer is fixed to the shaker plate to monitor the vibration of shaker, and the laser vibrometer measures the velocity of the cantilever.

The natural frequency of the beams is firstly measured by using an impact hummer (force transducer C9019) while the composite piezo beam is fixed at the clamp. The output of the force transducer and the laser vibrometer is generated through the M+P

VibRunner signal acquisition system (M+P international, Germany). To measure the power generation performance, the output voltage is measured by an oscilloscope (DSO 5034A, Agilent Technologies) with one channel.

The voltage response of the cantilever beam is acquired through a linear sweep at 0.5Hz/s, with frequency intervals obtained from the theoretical modal analysis for each stacking sequence considered (Table 5). The excitation acceleration of the shaker is controlled at 1g during the sweep excitations.

Results and discussions

Three-points bending test results

Figure 10 illustrates the load-displacements of the various composite structures. The curves associated to the positive and negative v_{13} can be divided into three parts: the first is a linear one related to the elastic deformation of the composite laminate; the second is indicative of a load drop because of the delamination of the CFRP laminate; the final one is related to the peak load and failure of the specimen. It is worth noticing that the laminates with near zero v_{13} ($[\pm 40^\circ / \pm 15^\circ]_s$, $[\pm 35^\circ / \pm 15^\circ]_s$) do not show an obvious onset for the delamination of the composite beams, and also the PZT layers appear to remain in good conditions after bending.

The flexural rigidity of the composite beams can be calculated using the 3-points bending curve (with the bending stiffness $YI = L^3 / 48 \left(\Delta F / \Delta f \right)$, where ΔF is the load difference at two given points on the linear part of the load-deflection curve, L the length of the beam and Δf is the corresponding displacement difference). The laminates with positive v_{13} ($[\pm 10^\circ / \pm 60^\circ]_s$) have the largest flexural rigidity

($0.23 Nm^2$), and the laminates with near zero v_{13} ($[\pm 40^\circ / \pm 15^\circ]_s$) show the minimum bending stiffness ($0.11 Nm^2$). For composite beams with similar dimensions and weight one could use laminates with near zero v_{13} to obtain composite PEHs with a small fundamental frequency and high compliance. The bending stiffness D_{11} of the composites beams with the PZT layer can be obtained from the 3-points bending results ($D_{11}=YI/b$), and also from the bending stiffness calculated with the FEA simulations. Figure 11 shows the deformed FE beams corresponding to the different stacking sequences. For the same 10N applied load the laminate with $[\pm 40^\circ / \pm 15^\circ]_s$ experiences the largest deflection ($0.76 mm$), and this is consistent with the experimental results. The patterns of the global countour displacements appear all similar between the different architectures, with only the maximum displacements different between them. Table 6 also lists the comparison between the experimental and FEA D_{11}. The major discrepancy between the two set of results occurs for the $[\pm 40^\circ / \pm 15^\circ]_s$ sequence, for which the experimental D_{11} ($5.5 Nm$) is 14.5% larger than the FEA one ($4.7 Nm$). Another notable discrepancy is the one related to the $[\pm 35^\circ / \pm 15^\circ]_s$ stacking sequence, for which the experimental D_{11} value is $6.6 Nm$, 10.8% larger than the FEA result ($5.9 Nm$). These two architectures are also the most compliant ones. For the other four laminates, the errors between the experimental and FEA results are however lower than 5%.

Vibration FRFs test results

The fundamental frequency and the damping ratio can be obtained from the FRF curve. One specimen is tested three times to acquire the fundamental natural frequency and

the average damping ratio. The results are listed in Table 7.

The results of the FRF test show that the fundamental frequency depends on the D_{11} of the laminates. The natural frequencies of the laminates with near zero v_{13} are relatively smaller than the positive Poisson's ratio ones. For example, the fundamental frequency of the clamped-free laminate $[\pm 40^{\circ}/\pm 15^{\circ}]_s$ ($v_{13}=-0.011$) is 118.6Hz, while for the laminates at $[\pm 10^{\circ}/\pm 60^{\circ}]_s$ ($v_{13}=0.305$) the same frequency is increased to 191.9Hz. The damping ratios of the cantilever beams do not appear to follow an obvious pattern. The damping ratios of the laminates with positive v_{13} are relatively smaller compared to the analogous values of the other four stacking sequences.

Figure 12 shows the voltage FRFs of the PEHs with the different configurations under linear sweep conditions (Table 5). The maximum voltage can be generated around the resonances, and the stacking sequences with near zero v_{13} experience a relatively lower (as expected) natural frequency.

The comparison between numerical and experimental results related to the maximum voltage FRFs and the resonance frequencies of the different PEHs are listed in Table 8. The results from the two different datasets agree well, and both the numerical calculations and the experimental results show that the laminates with near zero v_{13} have the lowest resonance frequencies and the highest voltage FRFs. For example, the experimental maximum voltage FRF of the PEH with stacking sequences of $[\pm 40^{\circ}/\pm 15^{\circ}]_s$ is 11.7V/g and occurs at 120.8Hz, while the FEA provides a 4.3% error with 11.2V/g. The experimental voltage FRFs are slightly different from the numerical results, but the overall error is still lower than 10%. For the laminates with negative v_{13}

($[\pm 25^{\circ}/\pm 25^{\circ}]_s$, $[\pm 20^{\circ}/\pm 30^{\circ}]_s$), the voltage FRFs are decreased to 10.9V/g and 11V/g respectively (experimental results) and the corresponding resonance frequencies are increased to 139.2Hz and 149.6Hz. The laminates with positive v_{13} ($[\pm 15^{\circ}/\pm 90^{\circ}]_s$, $[\pm 10^{\circ}/\pm 60^{\circ}]_s$) have peak values occurring at relatively higher frequencies than the other four laminates. The experimental results for these two stacking sequences (7.2V/g at 175.7Hz, 7.0V/g at 192.3Hz) are smaller than the ones provided by the FEA (7.5V/g at 171.3Hz, 7.1V/g at 179.5Hz).

The PEHs with near zero v_{13} show the best power generation properties compared with the PEHs with negative or positive v_{13} laminates. The maximum voltage FRFs of the PEHs with near zero v_{13} is 7.3% higher than the PEHs with negative v_{13}, and most importantly 62.5% higher than the one provided by the positive Poisson's ratio laminates. The 3-points bending test provide the evidence that the PEHs with near zero v_{13} have relatively low resonance frequencies. For different stacking sequences, PEHs designed with near zero v_{13} can sustain larger deformations and generate more power at relatively lower excitation frequencies.

Conclusions

This paper has been focusing on composite PEH architectures with a $[\pm\beta/\pm\theta]_S$ stacking sequence and their energy harvesting behavior. Theoretical calculations using Classical Laminate Theory show that the increase of balanced angles θ and β will contribute to reduce the elastic modulus E_1 and the bending stiffness D_{11}. With the increase of the ply angle β, the through thickness Poisson's ratio v_{13} first decrease then increases, and some specific stacking sequences can obtain negative (auxetic) or near zero values. The FEA results show that the two laminates with near zero v_{13} Poisson's ratio ($[\pm40^\circ/\pm15^\circ]_s$, $[\pm35^\circ/\pm15^\circ]_s$) can generate a higher voltage density than other four stacking sequences. We have also used a theoretical electro-mechanical model representing the dynamic behavior of a composite PEH and its voltage response under harmonic excitations. The three-points bending test results show the laminates with positive v_{13} ($[\pm10^\circ/\pm60^\circ]_s$) have the largest flexural rigidity, while and the laminates with near zero v_{13} experience the maximum compliance. Both the simulation and the experimental results show that the PEH with near zero v_{13} can generate the highest power compared with the PEHs with negative or positive v_{13} laminates. The results shown in this paper demonstrate the sensitivity of the design and performance of PEHs versus the through-the-thickness Poisson's ratios created by these particular stacking sequences. The results shown in Figures 7 and 8/12 are particularly interesting, because NZPR laminates appear to be quite suitable for power generation at low frequencies. It is also noticeable that both auxetic and NZPR laminates possess higher specific voltage densities than laminates with positive Poisson's ratio. Questions

however are open about the performance of other NZPR laminates with $[\beta/\theta]_s$ stacking sequences with marginally positive small angles, to verify whether there is any symmetry in the performance map of those PEHs versus the angle-ply architecture. The PEHs developed here are based on a single piezoelectric material patch, while some of the Authors have previously shown than different multilayer PZT architectures could be more beneficial in terms of normalized voltage output [26]; NPR and NZPR angle-ply configurations could therefore be explored also with those piezoelectric layers architectures. Nonetheless, the fact that auxetic and NZPR configurations provide larger voltage outputs at lower frequencies due to the higher compliance is a point worth of notice: PEHs at lower frequencies tend to be designed around systems with appended masses and in general of certain weight, while the laminates shown in this paper still possess lightweight characteristics that could provide equivalent performance compared to classical PEHs configurations, but lower emissions impact and constraints due to their smaller weight.

Acknowledgements

QL acknowledges the support of the National Natural Science Foundation of China (Grant Nos.: 11632005, 11672086, 11421091) and China Scholarship Council. FS is grateful to the logistic support from the MSCA ITN VIPER program regarding the use of the software and the access to the Material Laboratory of the Faculty of Engineering.

References

[1]. A. Alaimo, A. Milazzo and C. Orlando, Composite Structures 100 (5), 343-355 (2013).

[2]. M. Perton, B. Audoin, Y. D. Pan and C. Rossignol, Measurement Science & Technology 17 (12), R175-R195 (2006).

[3]. S. Roundy, P. K. Wright and J. Rabaey, Computer Communications 26 (11), 1131-1144 (2003).

[4]. J. A. Paradiso and T. Starner, IEEE Pervasive Computing 4 (1), 18-27 (2005).

[5]. N. S. Shenck and J. A. Paradiso, Micro IEEE 21 (3), 30-42 (2001).

[6]. H. S. Kim, J. H. Kim and J. Kim, International Journal of Precision Engineering & Manufacturing 12 (6), 1129-1141 (2011).

[7]. A. Erturk and D. J. Inman, Journal of Intelligent Material Systems & Structures 19 (19), 1311-1325 (2008).

[8]. A. Erturk and D. J. Inman, Journal of Vibration & Acoustics 130 (4), 1257-1261 (2008).

[9]. A. Erturk and D. J. Inman, Smart Materials & Structures 18 (2), 25009-25018 (2009).

[10]. M. P. Buric, G. Kusic, W. Clark and T. Johnson, presented at the Wireless and Microwave Technology Conference, 2006. Wamicon '06. IEEE, 2007 (unpublished).

[11]. A. Erturk, W. G. R. Vieira, C. De Marqui and D. J. Inman, Applied Physics Letters 96 (18), 043001 (2010).

[12]. H. A. Sodano, G. Park, D. J. Leo and D. J. Inman, presented at the Smart Structures and Materials 2003 Conference, 2003 (unpublished).

[13]. E. Erkan Aktakka, H. Kim and K. Najafi, Journal of Micromechanics & Microengineering volume 21 (21), 095016 (2011).

[14]. S. M. Shahruz, Journal of Sound & Vibration 292 (3–5), 987-998 (2006).

[15]. H. Xue, Y. Hu and Q. M. Wang, IEEE Transactions on Ultrasonics Ferroelectrics & Frequency Control 55 (9), 2104 (2008).

[16]. S. Qi, R. Shuttleworth, S. Olutunde Oyadiji and J. Wright, Smart Materials & Structures 19 (9), 094009 (2010).

[17]. L. Xiong, L. Tang and B. R. Mace, Applied Physics Letters 108 (20), 49 (2016).

[18]. L. Tang, Y. Yang and C. K. Soh, Journal of Intelligent Material Systems & Structures 21 (18), 1867-1897 (2010).

[19]. M. Ferrari, M. Bau, M. Guizzetti and V. Ferrari, Sensors and Actuators a-Physical 172 (1), 287-292 (2011).

[20]. R. L. Harne and K. W. Wang, Smart Materials & Structures 22 (2), 023001 (2013).

[21]. M. F. Daqaq, R. Masana, A. Erturk and D. D. Quinn, Applied Mechanics Reviews 66 (4) (2014).

[22]. A. F. Arrieta, P. Hagedorn, A. Erturk and D. J. Inman, Applied Physics Letters 97 (10) (2010).

[23]. Y. Shi, S. R. Hallett and M. Zhu, Composite Structures 160, 1279-1286 (2017).

[24]. M. Akbar and J. L. Curiel-Sosa, Composite Structures 153, 193-203 (2016).

[25]. A. Paknejad, G. Rahimi, A. Farrokhabadi and M. M. Khatibi, Composite Structures 154, 694-706 (2016).

[26]. Q Lu, L Liu, F Scarpa, J Leng, Y Liu, Composite Structures 201, 121-130 (2018)

[27]. K. W. Wojciechowski, A. Branka and M. Parrinello, Molecular Physics 53 (6), 1541-1545 (1984).

[28]. K.W. Wojciechowski, MOLECULAR PHYSICS, 61 (5) 1247-1258 (1987)

[29]. K.W. Wojciechowski, PHYSICS LETTERS A 137 (2) 60-64 (1989)

[30]. R S Lakes, Science 235 (4792), 1038-1040 (1987)

[31]. F. Scarpa, L. G. Ciffo and J. R. Yates, Smart Materials & Structures 13 (1), 49-56 (2004).

[32]. F. Scarpa and F. C. Smith, Journal of Intelligent Material Systems and Structures 15 (12), 973-979 (2004).

[33]. A. Alderson, J. Rasburn and K. E. Evans, Physica Status Solidi 244 (3), 817-827 (2007).

[34]. A. A. Pozniak, J. Smardzewski and K. W. Wojciechowski, Smart Materials and Structures 22 (8) (2013).

[35]. F. Scarpa, P. Panayiotou and G. Tomlinson, Journal of Strain Analysis for Engineering Design 35 (5), 383-388 (2000).

[36]. A. Lorato, P. Innocenti, F. Scarpa, A. Alderson, K. L. Alderson, K. M. Zied, N. Ravirala, W. Miller, C. W. Smith and K. E. Evans, Composites Science and Technology 70 (7), 1057-1063 (2010).

[37]. L D Peel, D W Jensen, Journal of Composite Materials 35(2), 96-137 (2001)

[38]. Y. J. Chen, F. Scarpa, Y. J. Liu and J. S. Leng, International Journal of Solids and Structures 50 (6), 996-1004 (2013).

[39]. Y. Chen, F. Scarpa, C. Remillat, I. Farrow, Y. Liu and J. Leng, Journal of Intelligent Material Systems and Structures 25 (6), 731-743 (2014).

[40]. X. Gong, J. Huang, F. Scarpa, Y. Liu and J. Leng, Composite Structures 134, 384-392 (2015).

[41]. C. Lira, F. Scarpa and R. Rajasekaran, Journal of Intelligent Material Systems and Structures 22 (9), 907-917 (2011).

[42]. W. A. Smith, presented at the Ultrasonics Symposium, 1991. Proceedings., IEEE, 1991 (unpublished).

[43]. M. Avellaneda and P. J. Swart, Journal of the Acoustical Society of America 103 (103), 1449-1467 (1998).

[44]. V. Y. Topolov and C. R. Bowen, Materials Letters 142, 265-268 (2015).

[45]. M. L. D. Bellis and A. Bacigalupo, Smart Material Structures 26 (2017).

[46]. M. Ouisse, M. Collet and F. Scarpa, Smart Material Structures 25 (11) (2016).

[47]. Kolpakov, A.G. J. Appl. Math. Mech. vol. 49, 739-745 (1985)

[48]. Sigmund, O. Int. J. Solids Struct. 31, 2313-2329 (1994).

[49]. W. G. Hoover, C. G. Hoover, Phys. Status Solidi B vol. 242, 585 (2005).

[50]. J. W. Narojczyk, K. W. Wojciechowski, Journal of Non-Crystalline Solids 356: pp.2026-2032 (2010).

[51]. Alderson, K. Nazaré, S. Alderson, A. Phys. Status Solidi B Basic Solid State Phys. vol. 253, 1279-1287 (2016) doi:10.1002/pssb.201600079.

[52]. Grima, J.N.; Attard, D.; Caruana-Gauci, R.; Gatt, R., Scr. Mater. 65, 565-568, (2011).

[53]. Azzopardi, K.M.; Brincat, J.P.; Grima, J.N.; Gatt, R. Phys. Status Solidi B Basic Solid State Phys. 252, 1486-1491 (2015) doi:10.1002/pssb.201552069.

[54]. Ho, D.T.; Park, S.; Kwon, S.; Han, T.; Kim, S.Y. Phys. Status Solidi B Basic Solid State Phys. 253, 1288-1294 (2016) doi:10.1002/pssb.201600017.

[55]. Wang, Y.C.; Shen, M.W.; Liao, S.M. Phys. Status Solidi B Basic Solid State Phys. 254, 1700024 (2017) doi:10.1002/pssb.201700024

[56]. J N Grima, M C Grech, J N Grima‐Cornish, R Gatt, D Attard, ANNALEN DER PHYSIK 530 1700330 (2018)

[57]. J N Grima, S Winczewski, L Mizzi, M C Grech, R Cauch, R Gatt, D Attard, K W Wojciechowski and J Rybicki, Adv. Mater., 27 1455-1459 (2015)

[58]. K.W. Wojciechowski, A. Alderson, A. Branka, K.L. Alderson, PHYSICA STATUS SOLIDI B-BASIC SOLID STATE PHYSICS, 242(3), 497-497 (2005)

[59]. K.W. Wojciechowski, F. Scarpa, J.N. Grima, A. Alderson, PHYSICA STATUS SOLIDI B-BASIC SOLID STATE PHYSICS 256(1) (2019)

[60]. C. T. Herakovich, Journal of Composite Materials 18 (5), 447-455 (1984).

[61]. C. T. Sun and S. Li, Journal of Composite Materials 22 (7), 629-639 (1988).

[62]. J. F. Clarke, R. A. Duckett, P. J. Hine, I. J. Hutchinson and I. M. Ward, Composites 25 (9), 863-868 (1994).

[63]. K. E. Evans, J. P. Donoghue and K. L. Alderson, Journal of Composite Materials 38 (2), 95-106 (2004).

[64]. K. L. Alderson, V. R. Simkins, V. L. Coenen, P. J. Davies, A. Alderson and K. E. Evans, Physica Status Solidi B-Basic Solid State Physics 242 (3), 509-518 (2005).

[65]. Y. J. Chen, F. Scarpa, I. R. Farrow, Y. J. Liu and J. S. Leng, Smart Materials and Structures 22 (4) (2013).

[66]. E. H. Harkati, A. Bezazi, W. Boukharouba and F. Scarpa, Physica Status Solidi B-Basic Solid State Physics 246 (9), 2111-2117 (2009).

[67]. A. Bezazi, W. Boukharouba and F. Scarpa, Physica Status Solidi B-Basic Solid State Physics 246 (9), 2102-2110 (2009).

[68]. J. N. Grima, L. Oliveri, D. Attard, B. Ellul, R. Gatt, G. Cicala and G. Recca, Advanced Engineering Materials 12 (9), 855-862 (2010).

[69]. K. Virk, A. Monti, T. Trehard, M. Marsh, K. Hazra, K. Boba, C. D. L. Remillat, F. Scarpa and I. R. Farrow, Smart Materials and Structures 22 (8) (2013).

[70]. Y. Chen, B.B. Zheng, M.H. Fu, L.H. Lan and W.Z. Zhang, Smart Materials and Structures 27 (4) (2018).

[71]. K. R. Olympio and F. Gandhi, Journal of Intelligent Material Systems and Structures 21 (17), 1737-1753 (2010).

[72]. J. Huang, Q. Zhang, F. Scarpa, Y. Liu and J. Leng, Composite Structures 152, 729-736 (2016).

[73]. J. Rong and L. Zhou, Materials Research Express 4 (4) (2017).

Figure Captions

Figure1. Symmetric laminate under axial loadings where 2h is the thickness

Figure 2. Influence of the angle θ on E_1 and D_{11}

Figure 3. Influence of orientation on the in-plane Poisson's ratio v_{12}

Figure 4. Influence of the stacking sequences on the through-the-thickness Poisson's ratios v_{13} and v_{23}

Figure 5. Finite element model of the composites beam with the PZT layer

Figure 6. The voltage distribution along the z-direction in the various laminates

Figure 7. The voltage density of the laminate cross section

Figure 8. FEA results of the voltage FRFs of the PEH with different stacking sequences.

Figure 9. Vibration experimental setup. (1) VENZO880 shaker control system and platform; (2) Single point laser Doppler vibrometer; (3) Control system of the Doppler vibrometer; (4) Test specimen with clamp; (5) M+P VibRunner signal acquisition system; (6) DSO 5034A oscilloscope; (7) Force hummer.

Figure 10. Three points bending test results

Fig. 11 FEA results of the 3-points bending laminates. (a) $[\pm 40^\circ / \pm 15^\circ]_s$; (b) $[\pm 35^\circ / \pm 15^\circ]_s$; (c) $[\pm 25^\circ / \pm 25^\circ]_s$; (d) $[\pm 20^\circ / \pm 30^\circ]_s$; (e) $[\pm 15^\circ / \pm 90^\circ]_s$; (f) $[\pm 10^\circ / \pm 60^\circ]_s$

Figure 12. Experimental swept sine results of the PEHs with different stacking sequences

Table Captions

Table 1. Properties of unidirectional IM7/8552

Table 2. Laminates stacking sequences

Table 3. Selected stacking sequences and their properties

Table 4. Properties of the PZT layer

Table 5. Vibration sweep frequencies of the specimens

Table 6. Comparisons between the experimental and numerical FEA D_{11} values.

Table 7. Fundamental frequency and damping ratio for the different stacking sequences

Table 8. Comparisons of the maximum voltage FRFs between the FEA and the experimental results.

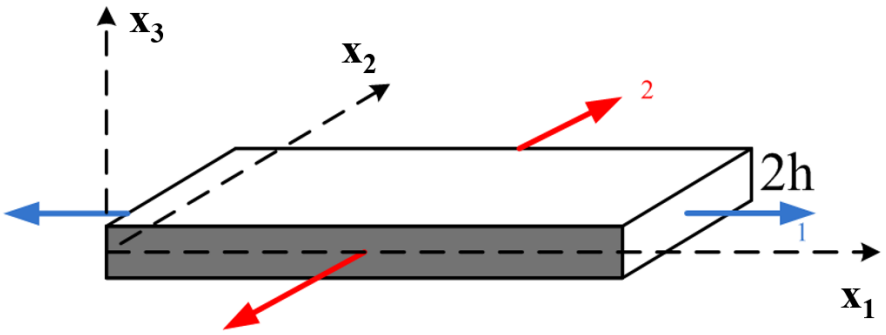

Figure1. Symmetric laminate under axial loading. The thickness here is equal to 2h

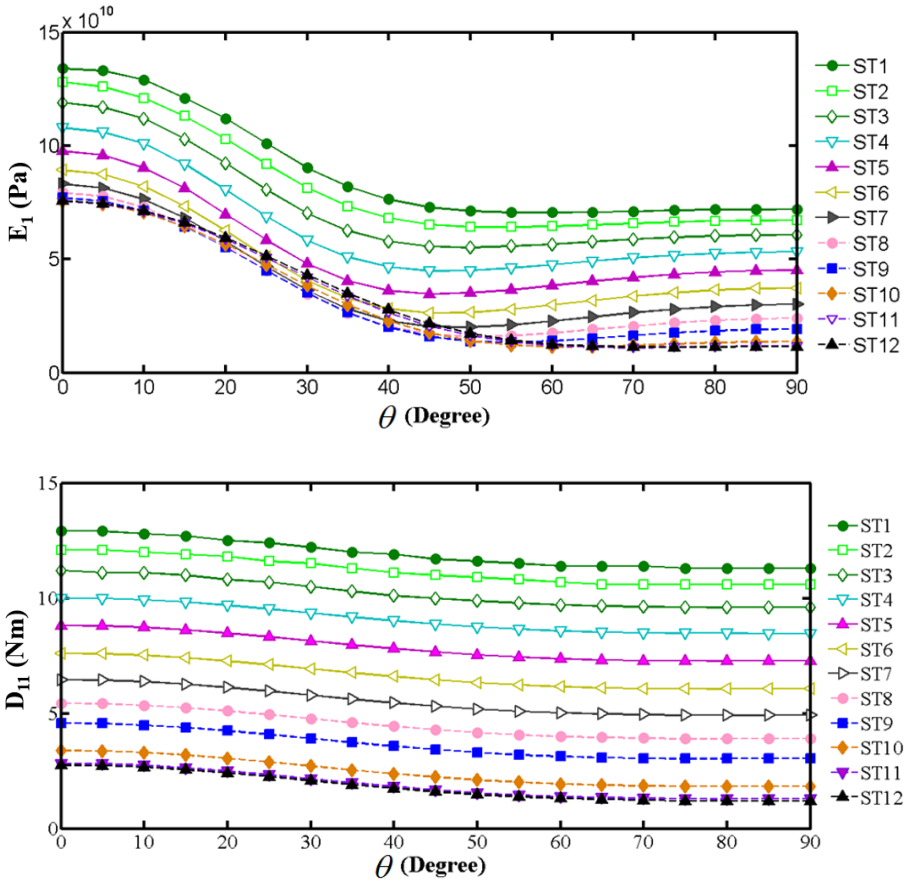

Figure 2. Influence of the angle θ on E_1 and D_{11}

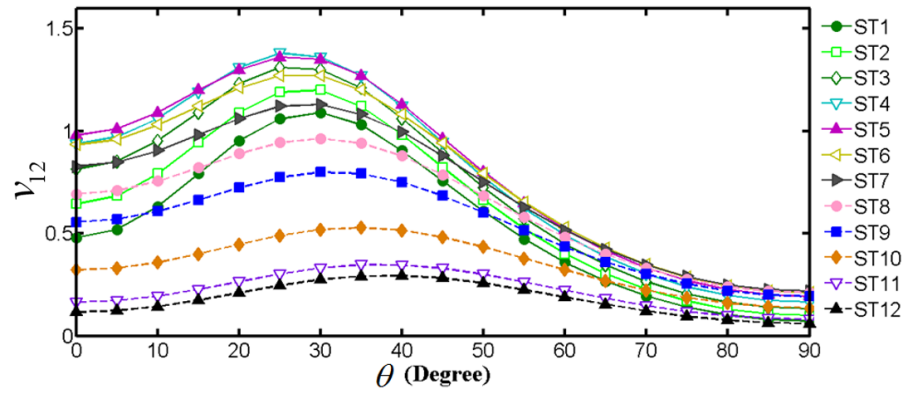

Figure 3. Influence of orientation on the in-plane Poisson's ratio ν_{12}

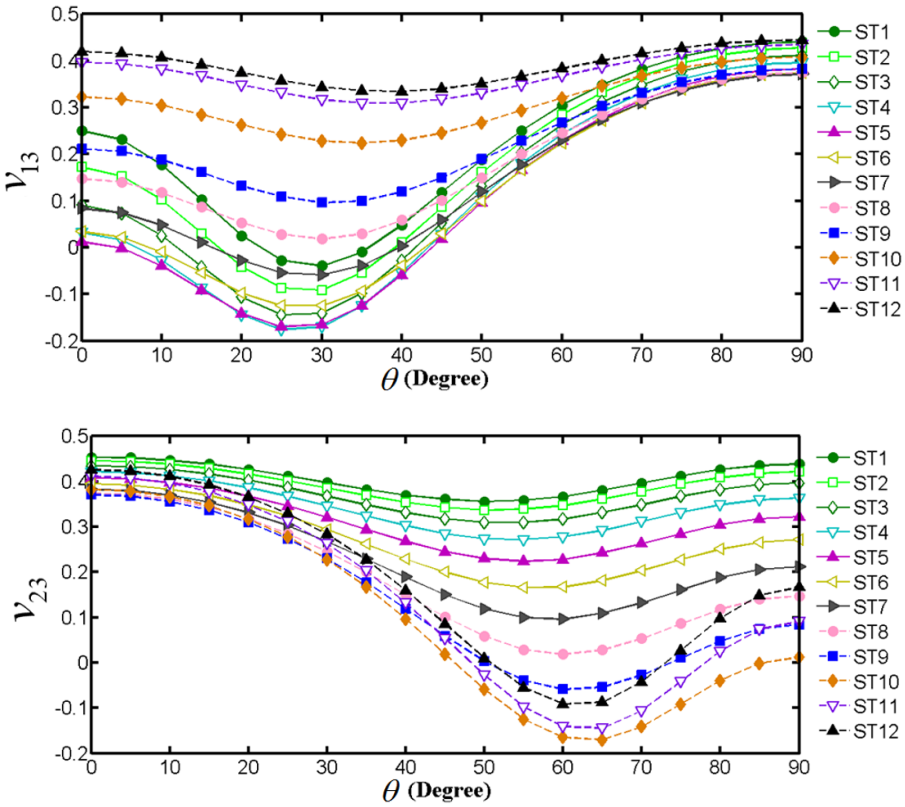

Figure 4. Influence of the stacking sequences on the through-the-thickness Poisson's ratios ν_{13} and ν_{23}

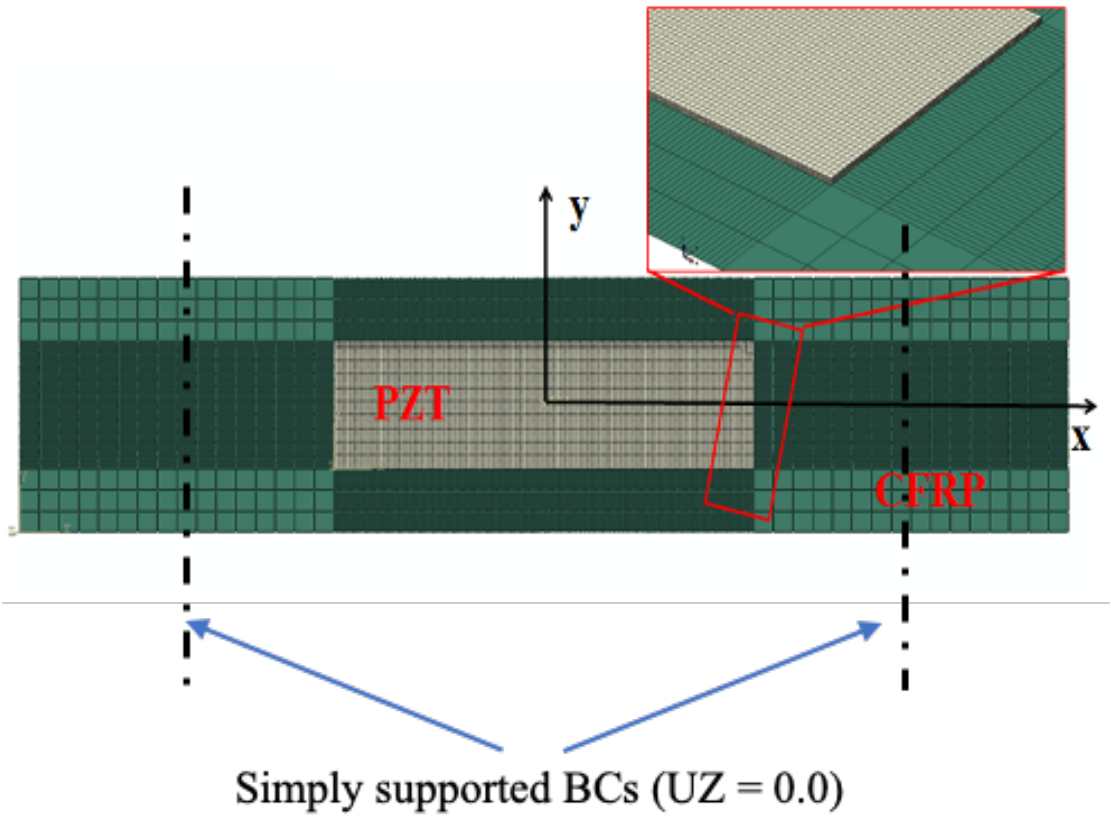

Figure 5. Finite element model of the composites beam with the PZT layer

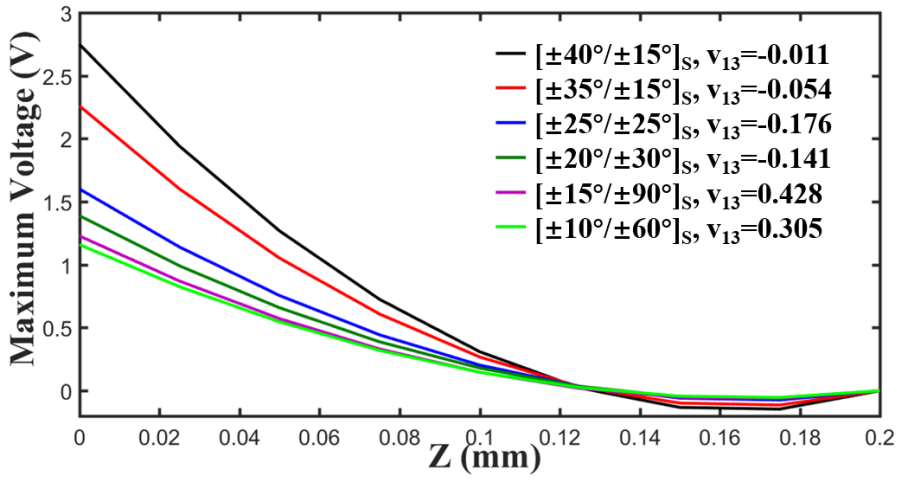

Figure 6. The voltage distribution along the z-direction in the various laminates

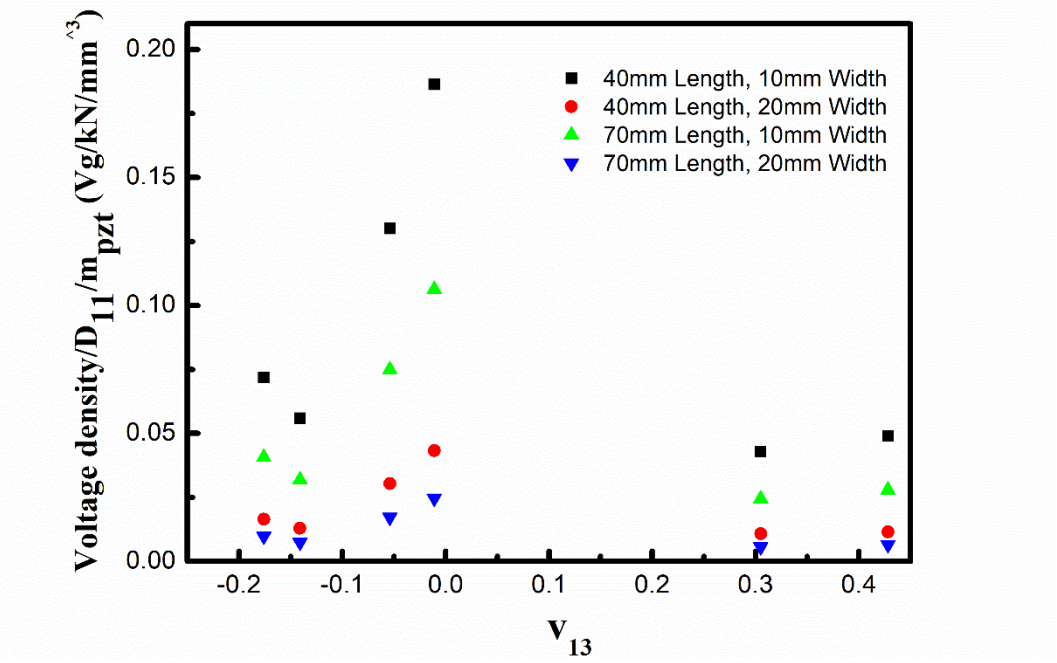

Figure 7. The voltage density of the laminate cross section

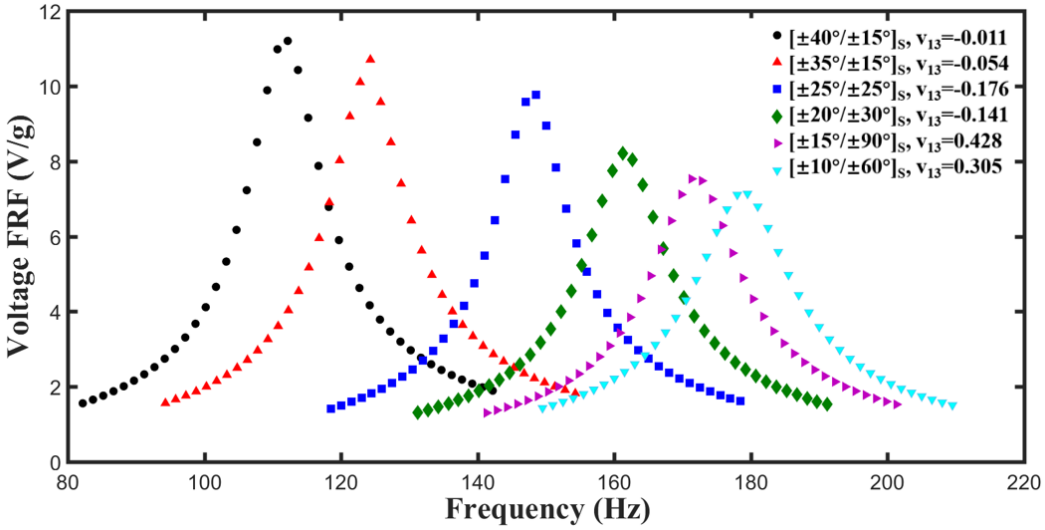

Figure 8. FEA results of the voltage FRFs of the PEH with different stacking sequences.

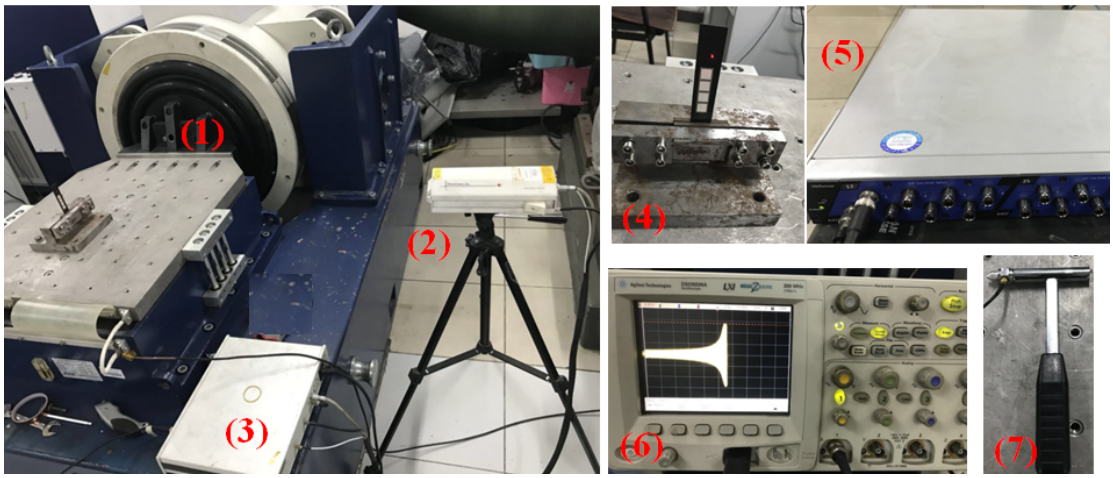

Figure 9. Vibration experimental setup. (1) VENZO880 shaker control system and platform; (2) Single point laser Doppler vibrometer; (3) Control system of the Doppler vibrometer; (4) Test specimen with clamp; (5) M+P VibRunner signal acquisition system; (6) DSO 5034A oscilloscope; (7) Force hummer.

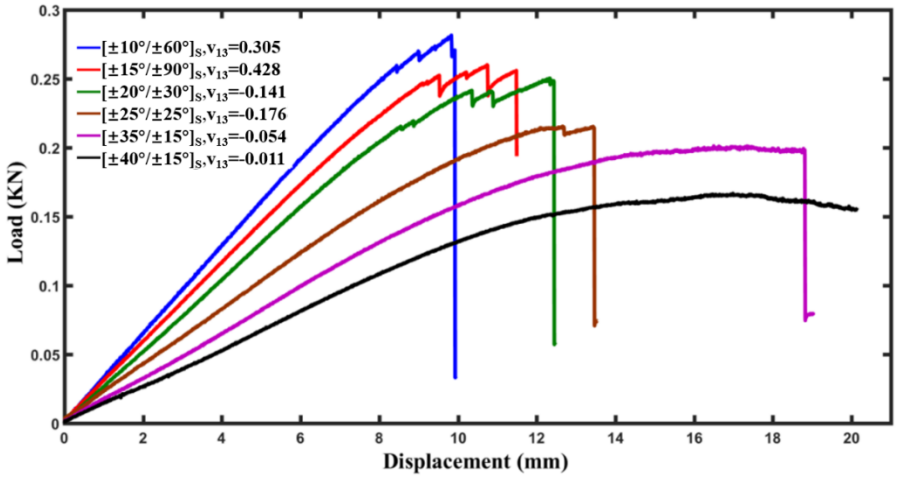

Figure 10. Three points bending test results

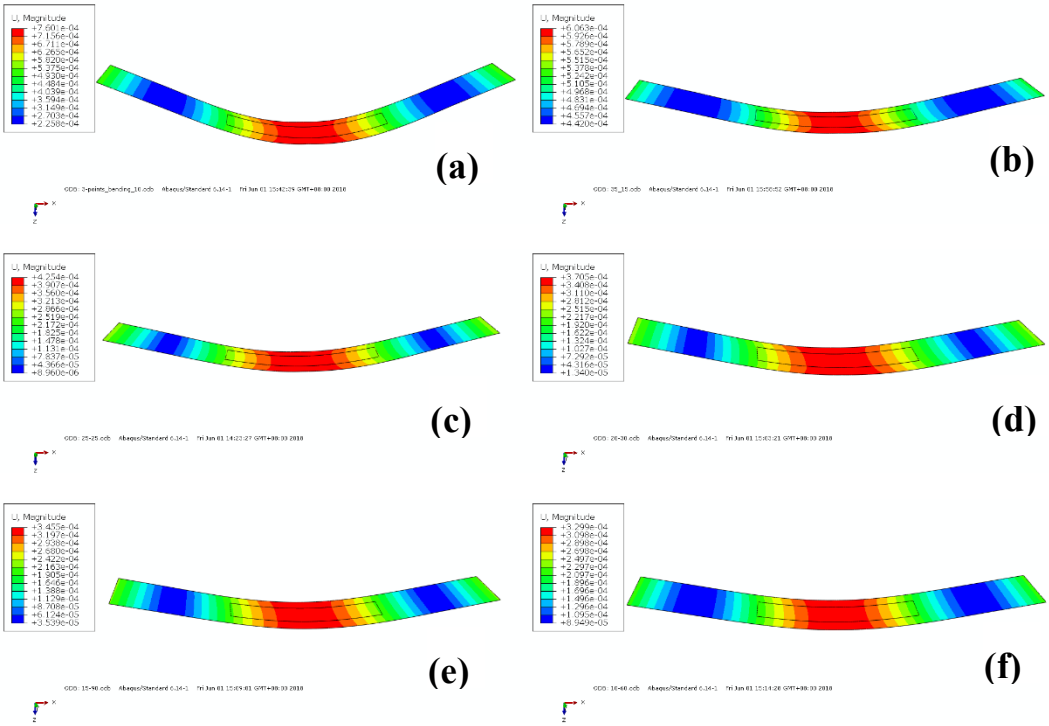

Fig. 11 FEA results related to the 3-points bending laminates. (a) $[\pm 40^\circ / \pm 15^\circ]_s$; (b) $[\pm 35^\circ / \pm 15^\circ]_s$; (c) $[\pm 25^\circ / \pm 25^\circ]_s$; (d) $[\pm 20^\circ / \pm 30^\circ]_s$; (e) $[\pm 15^\circ / \pm 90^\circ]_s$; (f) $[\pm 10^\circ / \pm 60^\circ]_s$

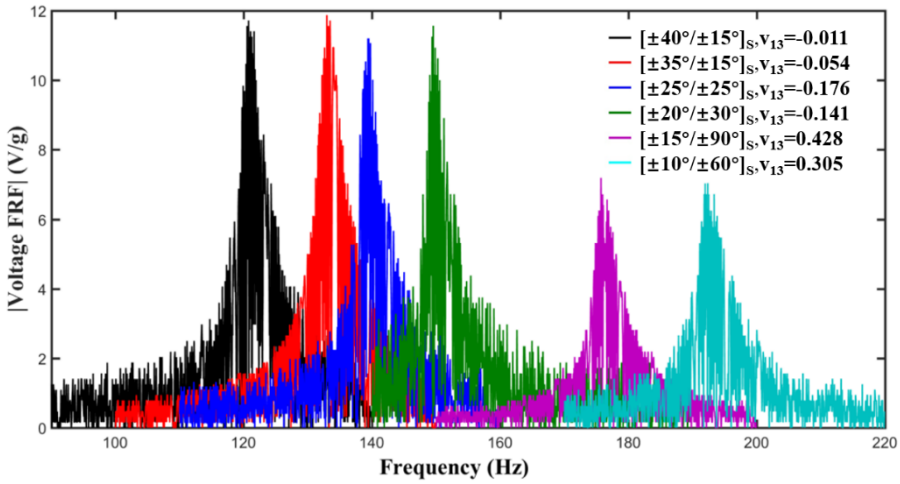

Figure 12. Experimental swept sine results of the PEHs with different stacking sequences

Table 1. Properties of unidirectional IM7/8552

E11 [*GPa*]	139.7	G23 [*GPa*]	3.898
E22 [*GPa*]	11.39	ν_{12}	0.3236
E33 [*GPa*]	11.39	ν_{13}	0.3236
G12 [*GPa*]	4.753	ν_{23}	0.461
G13 [*GPa*]	4.753	Thickness [*mm*]	0.131

Table 2. Laminates stacking sequences

Name	Stacking sequences	Name	Stacking sequences
ST1	$[\pm 10^\circ / \pm\theta]_s$	ST7	$[\pm 40^\circ / \pm\theta]_s$
ST2	$[\pm 15^\circ / \pm\theta]_s$	ST8	$[\pm 45^\circ / \pm\theta]_s$
ST3	$[\pm 20^\circ / \pm\theta]_s$	ST9	$[\pm 50^\circ / \pm\theta]_s$
ST4	$[\pm 25^\circ / \pm\theta]_s$	ST10	$[\pm 60^\circ / \pm\theta]_s$
ST5	$[\pm 30^\circ / \pm\theta]_s$	ST11	$[\pm 70^\circ / \pm\theta]_s$
ST6	$[\pm 35^\circ / \pm\theta]_s$	ST12	$[\pm 80^\circ / \pm\theta]_s$

Table 3. Selected stacking sequences and their properties

Stacking sequences	v_{13}	E_1
ST4-5 $[\pm 25^\circ / \pm 25^\circ]_s$	-0.176	68.8*GPa*
ST3-6 $[\pm 20^\circ / \pm 30^\circ]_s$	-0.141	70.2*GPa*
ST6-4 $[\pm 35^\circ / \pm 15^\circ]_s$	-0.054 (Near zero)	73.3*GPa*
ST7-4 $[\pm 40^\circ / \pm 15^\circ]_s$	-0.011 (Near zero)	68.1*GPa*
ST2-19 $[\pm 15^\circ / \pm 90^\circ]_s$	0.428	67.2*GPa*
ST1-13 $[\pm 10^\circ / \pm 60^\circ]_s$	0.305	70.5*GPa*

Table 4. Properties of the PZT layer

Properties	PZT-5H	Properties	PZT-5H
Density [kg/m^3]	7800	Modulus [*GPa*]	60.6
Length [*mm*]	40	Poisson's ratio	0.289
Width [*mm*]	10	Piezoelectric stress constants	-17.15

		[C/m^2]	
Thickness [mm]	0.2	Absolute permittivity [F/m]	3800

Table 5. Vibration sweep frequencies of the specimens

Specimens	Sweep frequencies
$[\pm 40^\circ / \pm 15^\circ]_s$	90Hz-140Hz
$[\pm 35^\circ / \pm 15^\circ]_s$	100Hz-150Hz
$[\pm 25^\circ / \pm 25^\circ]_s$	110Hz-160Hz
$[\pm 20^\circ / \pm 30^\circ]_s$	140Hz-190Hz
$[\pm 15^\circ / \pm 90^\circ]_s$	150Hz-200Hz
$[\pm 10^\circ / \pm 60^\circ]_s$	170Hz-220Hz

Table 6. Comparisons between the experimental and numerical FEA D_{11} values.

Specimens	Experimental D_{11} [Nm]	FEA D_{11} [Nm]	Error
$[\pm 40^\circ / \pm 15^\circ]_s$	5.5	4.7	14.5%
$[\pm 35^\circ / \pm 15^\circ]_s$	6.6	5.9	10.8%
$[\pm 25^\circ / \pm 25^\circ]_s$	8.2	8.4	2.4%
$[\pm 20^\circ / \pm 30^\circ]_s$	9.3	9.6	3.1%
$[\pm 15^\circ / \pm 90^\circ]_s$	10.2	10.3	1%
$[\pm 10^\circ / \pm 60^\circ]_s$	11.4	10.9	4.4%

Table 7. Fundamental frequency and damping ratio for the different stacking sequences

Specimens	Average Fundamental frequency (Hz)	Average damping ratio
$[\pm 40^\circ / \pm 15^\circ]_s$ $\nu_{13} = -0.011$	118.6	0.0062

$[\pm 35^\circ / \pm 15^\circ]_s$ $v_{13} = -0.054$	133.6	0.0060
$[\pm 25^\circ / \pm 25^\circ]_s$ $v_{13} = -0.176$	138.5	0.0053
$[\pm 20^\circ / \pm 30^\circ]_s$ $v_{13} = -0.141$	156.3	0.0068
$[\pm 15^\circ / \pm 90^\circ]_s$ $v_{13} = 0.428$	169.7	0.0041
$[\pm 10^\circ / \pm 60^\circ]_s$ $v_{13} = 0.305$	191.9	0.0037

Table 8. Comparisons of the maximum voltage FRFs between the FEA and the experimental results.

Stacking sequences	FEA results		Experimental results	
	1st frequency [Hz]	Voltage FRF [V/g]	1st frequency [Hz]	Voltage FRF [V/g]
$[\pm 40^\circ / \pm 15^\circ]_s$	112.2	11.2	120.8	11.7
$[\pm 35^\circ / \pm 15^\circ]_s$	124.3	10.7	132.9	11.8
$[\pm 25^\circ / \pm 25^\circ]_s$	148.5	9.8	139.2	10.9
$[\pm 20^\circ / \pm 30^\circ]_s$	161.2	8.2	149.6	11
$[\pm 15^\circ / \pm 90^\circ]_s$	171.3	7.5	175.7	7.2
$[\pm 10^\circ / \pm 60^\circ]_s$	179.5	7.1	192.3	7.0